Wear-estimation law based on debris-level origins using a diamondlike-carbon head

Fan Zhang,[1] Yu Wang,[1,*] Yueqiang Hu,[2] Mingquan Zhang,[1] and Baotong Li[1]

[1] *School of Mechanical Engineering, Xi'an Jiaotong University, Xi'an 710049, China*

[2] *National Research Center for High-Efficiency Grinding, College of Mechanical and Vehicle Engineering, Hunan University, Changsha 410082, China*

(Received 16 March 2024; revised 8 August 2024; accepted 7 October 2024; published 4 March 2025)

Diamondlike-carbon (DLC) films are widely used as nanocoatings in devices such as in hard disk drives. However, the narrow spacing causes collisions between the head and disk and leads to wear of the nanocoatings. Herein, the nanoscale wear estimation approach during DLC head sliding is investigated. The molecular dynamics (MD) method is applied to create a systematic interface model that explores how the wear mechanisms of the DLC head transform. The mechanisms of wear debris formation are discussed by analyzing the corresponding spatial distributions. Based on the clear fundamental debris-level origins of the MD simulation, an improved wear law is proposed for time-resolved adhesive wear estimation at the nanoscale. The proposed law establishes a connection between the measurable quantity, that is, normal stress, and the height loss. It is applied to quantify the head's height loss and additional simulations involving different external loads are performed to verify the applicability of the proposed wear law.

DOI: 10.1103/PhysRevApplied.23.034005

I. INTRODUCTION

With the development of nanotechnology, the issue of wear has become extremely critical, particularly in nanoelectromechanical systems. Diamondlike-carbon (DLC) films are widely used as protective nanocoatings, for instance, in magnetic storage devices, owing to their polymorphic nature [1]. The head-disk interface clearance of the hard disk drive (HDD), a significant magnetic storage device, is on the order of several nanometers [2]. This narrow clearance increases the probability of frequent collisions when the disk is driven at high rotation speeds. After these encounters, the protrusion comes into rubbing contact with the disk. This is a common reason for adhesive wear, regardless of the presence of a lubricant [3].

The adhesive wear issue has been studied for nearly a century. In 1946, Holm [4] first proposed the adhesive wear model, and, shortly after, Archard [5] provided a concise expression to estimate the worn volume, which has been used extensively ever since [6–8]. These empirical models, which have undergone several runs of modification and verification over the years, have worked well at the macroscale. However, with the rapid development of nanoscale imaging methods, such as atomic force microscopy [9], transmission electron microscopy [10], and scanning electron microscopy [11], material wear mechanisms can now be pictured at the nanoscale. Various experiments [7,12,13] have demonstrated the ineffectiveness of the direct application of the macroscale wear models [14] at the atomic scale. Moreover, with the aid of molecular dynamics (MD) technology, which is uniquely suited to complement experimental characterization by tracking each atom, the ineffectiveness of the aforementioned models has been reconfirmed by atomistic simulations [15–17]. Breakdown occurs primarily due to the wear mechanisms at the atomic scale for the Archard wear law, namely atom-by-atom removal and fracture, but not plasticity.

Head wear is an indication of DLC material removal since the head is shielded by DLC. Over the years, the wear mechanism of DLC has been investigated both theoretically and experimentally [18–21]. The tribological properties of DLC depend on the ratio of sp^2 to sp^3 structures. Nonhydrogenated DLC is used as a protective layer for the magnetic head [22]. In order to examine the DLC wear mechanism, the majority of investigations on the material have involved moving a tip across a substrate. For instance, Bai *et al*. [23] proposed that as roughness increases, adhesive wear transforms to abrasive wear. For flat surfaces, Dai *et al*. [24] found that the wear mechanism changes from atom-by-atom to cluster wear as the load increases. Furthermore, high load pressure, which induces shear strain in the tip, can lead to phase transformation and improve the graphitization level [25,26]; this may help

*Contact author: ywang95@xjtu.edu.cn

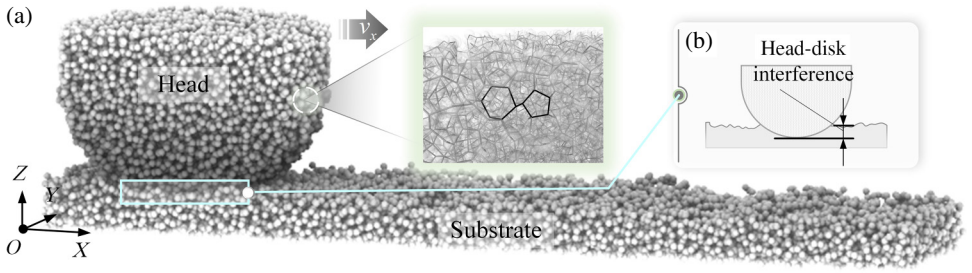

FIG. 1. Schematic of head-substrate system. (a) Diamondlike-carbon (DLC) head, bonded mainly by sp^2 and sp^3 bonds, shown with the pentatomic and hexahydric rings in the panel, slides at a constant speed against the DLC substrate and maintains a set head-disk interference during sliding. (b) Diagram of head-disk interference.

improve the tribological properties. Sha *et al.* [27] performed a large-scale MD simulation of DLC wear. The results indicated detachment of a "tail" from the tip during the wear process and demonstrated the applicability of Archard's model at the nanoscale. However, Bhaskaran *et al.* [11] demonstrated the failure of this model after a certain sliding distance. Nonetheless, the applicability of macroscale wear models at the nanoscale is worth studying. In previous studies, a constant load was always applied at the tip to ensure stable interaction between the tip and substrate. However, for an HDD, the head flies at a set height, and the load between head and substrate changes as the head wears. Therefore, considering the stress releases [7] induced by wear removal during sliding and the forces transmitted between the material and its surroundings, which are important in wear evaluation [27], an applicable wear law is pursued to evaluate DLC head wear during sliding. To study the sliding process under a variable load, the MD method is applied to build a wear model for investigating the wear behavior of a DLC head.

In this study, a wear model is established to explore the wear mechanism of a DLC head sliding against a DLC surface. The head wear behavior is investigated at different head-disk interferences. By analyzing the spatial distribution of wear debris, the debris is grouped into three types, and the wear mechanism of the DLC head is clarified from the atomic perspective. A quantitative analysis of the DLC head's height loss reveals that the combined Barwell model works well for time-resolved head wear estimation. Finally, an improved wear law is proposed based on the combined model to enhance the applicability of the Barwell law, which is verified by additional simulation under applied external loads.

II. METHODOLOGY

As illustrated in Fig. 1(a), a wear model is constructed using the MD approach to investigate the wear mechanism of the DLC head during sliding. The DLC is typically modeled using the liquid quenching technique [28–30], and our model adopts the nonhydrogenated structure used by Price and Raeymaekers [22] and Sha *et al.* [27]. It is well known that surfaces have many asperities and are inherently rough. Since contact occurs at the asperity contact zone, roughness is a significant factor in tribological behavior [31]. The substrate is modeled as having a rough surface to account for this. Details (including force field, system size, verification of model validity, and so forth) of the modeling approach are supplied in Appendix A. In the modeled system, periodic boundary conditions are applied to the lateral X-Y plane. Along the Z coordinate, all atoms within 3 Å of the bottom of the substrate are boundary atoms and fixed, and those within 2 Å above the fixed layer are maintained as a thermostatic layer (300 K). The remaining atoms in the substrate, defined as the Newtonian layer, move freely according to classical dynamics. For the head, those atoms within the top 15 Å are boundary atoms and kept away from the movement during sliding. The snapshots of the later visualization are obtained from OVITO [32].

There are two stages of the overall simulation process. In the first stage, the head is positioned far away from the substrate to avoid initial interaction, and then it travels closer to the substrate until it reaches a constant height. Because the head flies at a certain height while the HDD is operating, a range of head-disk interferences measured as shown in Fig. 1(b) is set. Here, the head-disk interference has a step of 1 Å from −10 Å to −4 Å, with an additional interference of −2 Å. The second stage begins after thermal equilibrium. A horizontal velocity ($v = 5$ Å/ps) is applied along the X coordinate to the head, whose top surface's height remains unchanged. This speed is approximately 5 times faster than that of enterprise-level hard drives, but this speed has been proven to be feasible, as shown in the results provided by Fig. 13 of Appendix B, thus allowing a reduction in processing time. Owing to the elastic and plastic deformation that occurs during sliding, wear debris derives from the shear zone and mass transfer is triggered across the interface. These debris can be recognized by measuring the velocity of atoms [33,34]. Atoms with momentary velocities less than $0.1v$ are labeled as debris, because they separate from the head and adhere to

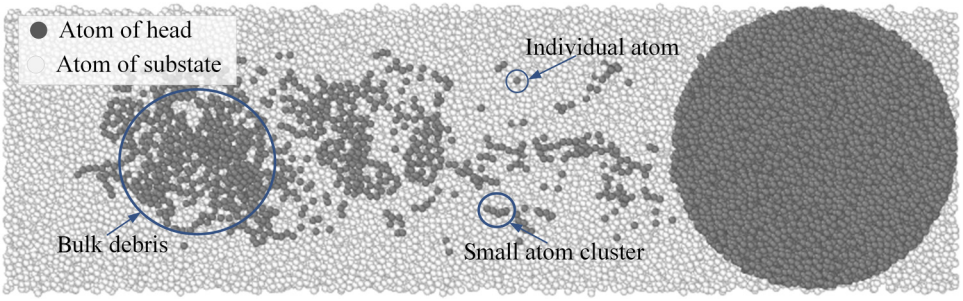

FIG. 2. Simulation results of sliding wear with head-disk interference of −6 Å.

the substrate, as stated in Ref. [34]. However, occasional misclassification may result if the momentary velocity of the debris exceeds the velocity threshold due to thermal motion. Herein, the velocity is integrated in the time domain to convert it into a displacement using a factor of n, that is, 0.1 nv, where n is the recorded time interval. The position of each atom is recorded at intervals of $n = 0.3$ ps. Consequently, the debris is distinguished by computing the displacement difference over the recorded time interval and contrasting it with the displacement threshold; if the displacement difference is smaller than the threshold, the atom is classified as wear debris.

III. RESULTS AND DISCUSSION

A. Debris-level origins of the DLC head's wear mechanism

The DLC head's wear mechanism is analyzed in this section as it slides under different head-disk interferences in its inception.

Snapshots of the simulation results obtained at a head-disk interference of −6 Å are shown in Fig. 2. The phenomenology results are analyzed at first. Three types of wear debris are distinguished from the illustration: individual atoms, small atom clusters, and bulk debris, as reported in Refs. [24,35]. For the formation of individual atom debris, mass transfer is triggered by atom-by-atom removal, which can be explained using the thermal activation theory [36]. Dangling bonds are present on the counterfaces and they could form the interfacial C—C bonds in the contact regime. The interfacial C—C bonds are sheared and broken and debris is generated as the head slides. Three bond-breakage cases were presented in Ref. [24]. By tracking the trajectories of individual atom debris, the types "atom C detaches" and "bond β breaks" proposed in the literature are given in Fig. 3. Since the "bond α breaks" type does not influence the head's mass loss, it is not discussed here. This atom-by-atom wear mechanism has also been reported in a previous study [37]. As for the formation of small atomic clusters, they preferentially detach from the head via "tail" fracture [27]. Atoms are transported to the tail end of the head-substrate contact interface during sliding and accumulate along the head's trailing edge as a result of shear force, giving the clusters the appearance of a tail. Then the clusters detach as wear debris. The mass loss of the head is lower for both individual atom debris and small atom cluster debris compared with that for bulk debris, and therefore,

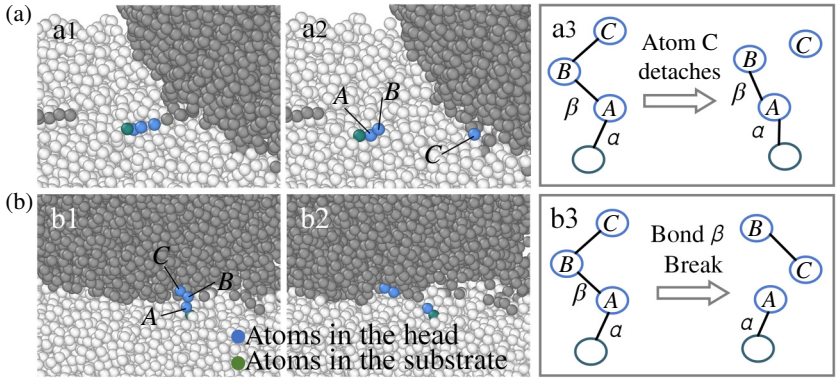

FIG. 3. Atomic tracking of atom-by-atom wear. Three connected atoms (blue balls) in the head bond with an atom (green ball) in the substrate and form a chain. (a) One type of the atom-by-atom wear mechanism ("atom C detaches", i.e., atom C detaches from the chain, and atoms A and B become debris). (b) Another type of the atom-by-atom wear mechanism ("bond β breaks", i.e., atoms C and B detach from the chain, atom A becomes debris).

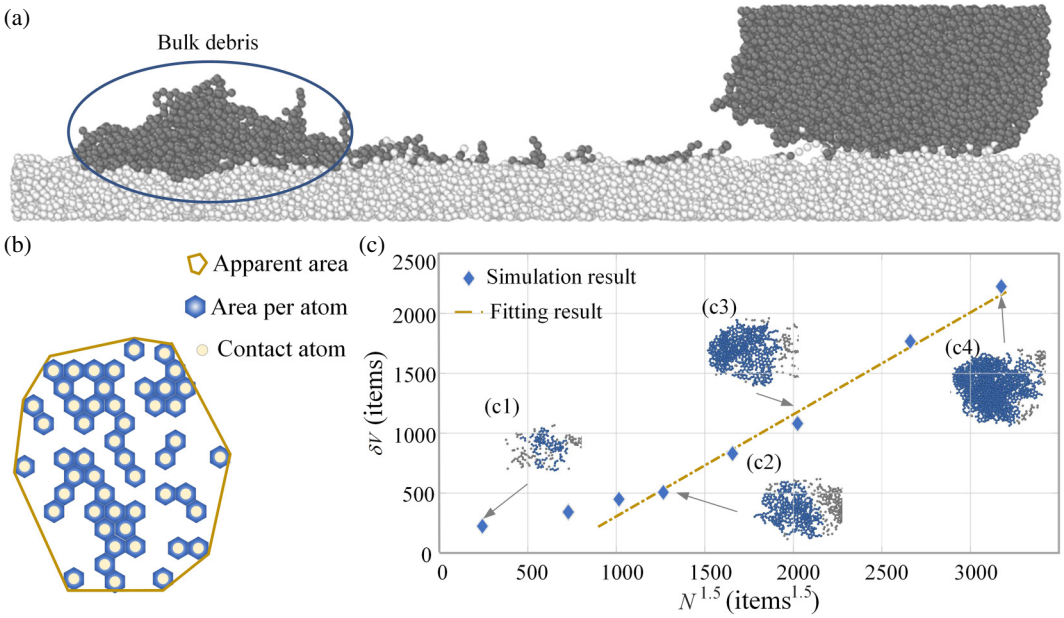

FIG. 4. Plastic deformation fracture mechanism. (a) The molecular dynamics (MD) simulation (section view). (b) Schematic of apparent and real contact area. Apparent contact area is defined as the envelope of the contact zone and real contact area is the sum of each contact atom area. (c) Relationship between material lump removal volume and contact size (diamond dots). The blue atoms in the illustrations (c1)–(c4) represent the bulk debris.

the two former wear behaviors are defined as atomic wear.

The results corresponding to the head-disk interference of −10 Å for the bulk debris production are shown in Fig. 4(a). Strong interfacial adhesion at the start of sliding causes the head to weld to the substrate; this process is known as cold welding [16]. A dissipation mechanism, plasticity here, is required to dissipate the tangential work applied to the head. With continued sliding, the internal stress of the junction continues to increase until plastic fracture occurs. The entire process is called plastic wear. For the plasticity-dominated wear mechanism, the assumption of Archard's wear law [5] proposes that the lump removal volume δV is proportional to the cube of the contact size (contact radius a here), i.e., $\delta V \propto a^3$. However, the definition of "contact" is ambiguous at the atomic scale. Fortunately, a method based on interfacial chemical bonds [38,39] is proposed and applied herein. The real contact area, proportional to the number of contact atoms N, is applied rather than the apparent area, as illustrated in Fig. 4(b). So, we can get $a \sim N^{0.5}$, which leads to $\delta V \propto N^{1.5}$. To quantify the volume of wear debris, the number of lost atoms is applied, owing to its independence of the debris shape.

The relationship between $N^{1.5}$ and δV is depicted in Fig. 4(c). When the head-disk interference is less than −5 Å, which means stronger adhesion between the head and substrate, a good linear relationship exists between them. This demonstrates the validity of Archard's wear law in plastic wear, and a similar result was reported in Ref. [7]. However, when the head-disk interference is greater than −5 Å, this law fails in the case of weaker adhesion. Failure, in our opinion, is caused by the indistinguishable source of wear debris. As Fig. 4(c1) illustrates, debris makes up a fraction of the cluster and plastic-wear-induced debris does not dominate. The debris caused by both atomic and plastic wear binds together to form a cluster. Therefore, the atomic loss number derived from the simulation results is greater than that derived from the fitting findings of Archard's wear law.

Since the debris is divided into three types, the spatial distributions of these debris types are analyzed and given in Fig. 5. Notably, an important aspect of this process is debris cluster identification. For cluster identification, a cutoff $R_c = 2.1$ Å is used in accordance with the Tersoff potential [40]. If the distance between two atoms is less than R_c, they belong to the same cluster, otherwise they are grouped into different cluster. Because no extra mass transfer occurs in the region where the head can slide, the type of debris indicates the wear mechanism of the head as it is sliding and the spatial distribution of all debris implies how the wear mechanism transforms during sliding. As shown in Fig. 5, at the beginning of sliding (20–80 Å along the X coordinate), the debris whose atomic counts exceed 50 appear, so the debris during this period are dominated by bulk debris, meaning that plastic wear is dominant. As sliding continues, individual atoms or small atom cluster debris, whose atomic counts are less than 10 (140–200 Å

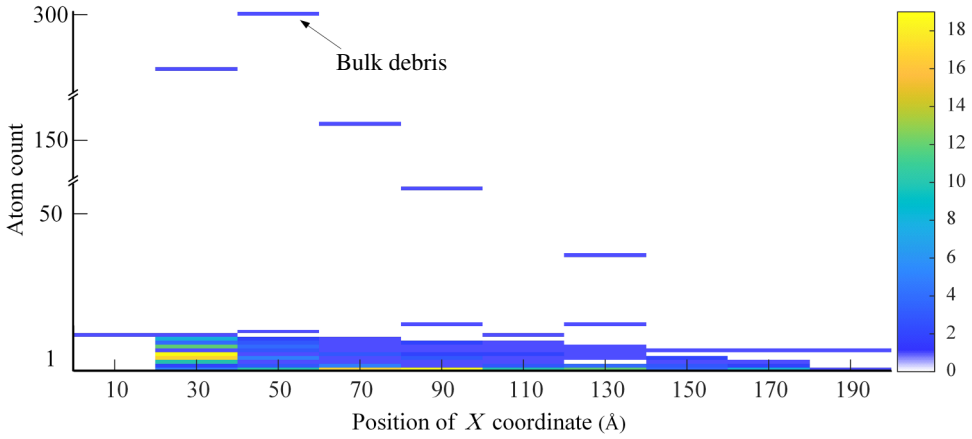

FIG. 5. Spatial distribution of wear debris. The atom count refers to the number of atoms in a cluster and the color bar indicates the number of debris clusters.

along the X coordinate), are formed, which means the wear mechanism is atomic wear. This outcome indicates that the wear mechanism transforms from plastic wear to atomic wear during sliding. The transformation explains the failure of Archard's law after a certain sliding distance [15] because of the atomic wear mechanism.

B. Wear estimation of the sliding head

In HDDs, the gap between the head and disk determines the read/write performance, especially the magnetic recording density. Thus, the wear height loss h_r of the head tip, defined as the reduction of worn tip surface height compared to the initial tip surface height, is quantified to estimate head wear. The measured wear height losses of all the interference cases are plotted in Fig. 6.

The height loss is severe at the beginning of sliding, that is, during the "wear-in" process, and becomes slight as sliding continues. Therefore, the entire wear process is described in terms of the wear-in and gradual-steady regimes. It is found that the combined Barwell law [34,41] is practicable for wear estimation with a time-dependent load and is described as follows:

$$h(t) = \omega_0 \tau \left[1 - exp\left(-\frac{t}{\tau}\right)\right] + \omega_c t, \tag{1}$$

where $h(t)$ is the height loss over time, ω_0 is the wear rate at the initial time, and τ is the time constant associated with the wear-in period. Another parameter ω_c is the steady-state wear rate. The combined law is applied to describe wear degradation of the head, as shown in Fig. 6. This law holds at the nanoscopic scale for wear estimation. Notably, it is an empirical law and there are three parameters, i.e., ω_0, τ, and ω_c, that need to be fitted. We try to reduce the number of fitting parameters and expand Barwell law's applicability according to the debris-level origins.

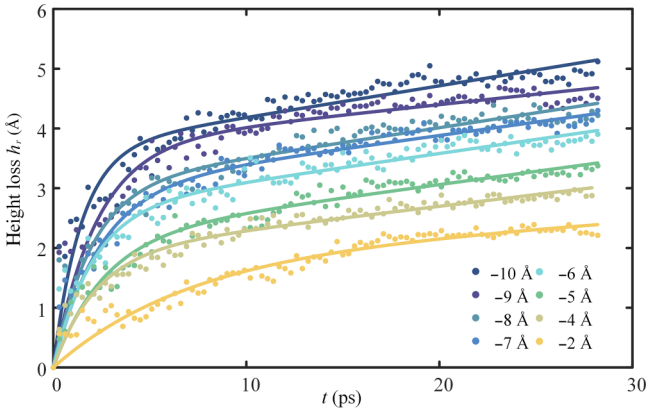

FIG. 6. Variation in height loss of the head during sliding obtained from MD simulations (solid points) for various head-disk interferences, along with the fitting curves obtained by applying the Barwell law (solid lines).

The first term in Eq. (1) is related to the wear-in period. According to analysis of spatial distribution, plastic wear dominates during this period. In Sec. III A, the applicability of Archard's wear law is verified for plastic wear. The wear volume is proportional to the applied load and given by [5]

$$W = KsP/p_m, \tag{2}$$

where W is the wear volume, s is the sliding distance, P is the applied load, p_m is the flow pressure, and K is a constant. Thus, the volume rate per unit sliding distance is $\partial W/\partial s$. The height wear rate per unit time is derived from the volume rate by applying a factor of the contact area A and expressed as follows:

$$\omega_w = \frac{\partial h}{\partial t} = \frac{v\partial W}{A\partial s} = \frac{Kv}{p_m} \cdot \frac{P}{A} = Kv\sigma_n/p_m, \tag{3}$$

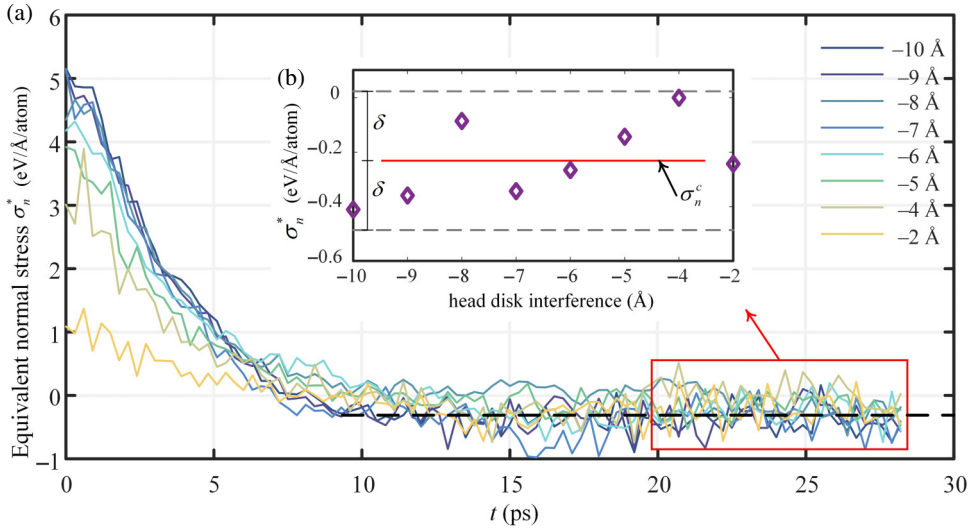

FIG. 7. Variation of stress between the head and disk over time. (a) Stresses corresponding to different head-disk interferences during sliding. (b) Mean stress of each interference case. Diamonds denote the means of stress of each head-disk interference and the solid red line denotes the mean of stress of all the head-disk interferences in the last 10 ps, δ denotes the standard deviations of these mean stresses.

where t is the time taken for sliding distance s, σ_n is the normal stress, and v is the sliding speed. When keeping the sliding speed constant, the coefficient $B = Kv/p_m$ can be obtained by fitting the MD simulation data, and the results are given in Fig. 14. Therefore, the initial wear rate ω_0 in the Barwell law is calculated by $\omega_0 = Kv\sigma_n^0/p_m$, where σ_n^0 is the initial normal stress during sliding.

The second term in the combined law depends on the steady state of the sliding process. In this period, according to the previous phenomenology analysis, wear debris is generated by atomic wear, which is a thermally activated and stress-assisted chemical bond breaking process [37] and the rate of atom loss is given by

$$\Gamma = k_0 exp\left(-\frac{\Delta U_{\text{act}} - \sigma_n \Delta V_{\text{act}}}{K_B T}\right), \tag{4}$$

where k_0 is a prefactor, ΔU_{act} is the internal energy of activation, ΔV_{act} is activation volume, K_B is the Boltzmann constant, and T is the temperature. Here, for a sphere, when the loss in height is small, the relationship between the loss in volume and the loss in height can be approximated as linear (Fig. 14 in Appendix C), and the loss in volume is proportional to the number of atoms lost. Thus, the height wear rate induced by the wear mechanism is written as follows:

$$\omega_s = k_s \Gamma + k_b, \tag{5}$$

where k_s is the ratio coefficient, and k_b the bias, such that the steady-state wear rate ω_c in Eq. (1) can be replaced by ω_s. Note that the height wear rates corresponding to both ω_w and ω_s depend on the normal stress σ_n. Therefore, the normal stress during sliding is measured and sketched in Fig. 7(a).

Equivalent normal stress is applied and obtained as $\sigma_n^* = F_z/N$. F_z is the normal force of the fixed layer of the head and N is the contact atomic number. At the start of sliding, interference occurs between the two counterfaces and causes deformation of both the head and substrate, which leads to repulsive stress. Stress is released as the

TABLE I. Values of parameters used in proposed wear law.

	Value							
Parameter	−10 Å	−9 Å	−8 Å	−7 Å	−6 Å	−5 Å	−4 Å	−2 Å
σ_n^0(eV/Å/atom)	4.980	4.795	4.704	4.630	4.263	3.973	3.170	2.227
ω_s^c(Å/ps)	0.0618							
σ_n^c(eV/Å/atom)	−0.2313							
B (Å · per atom/eV)	0.2427							

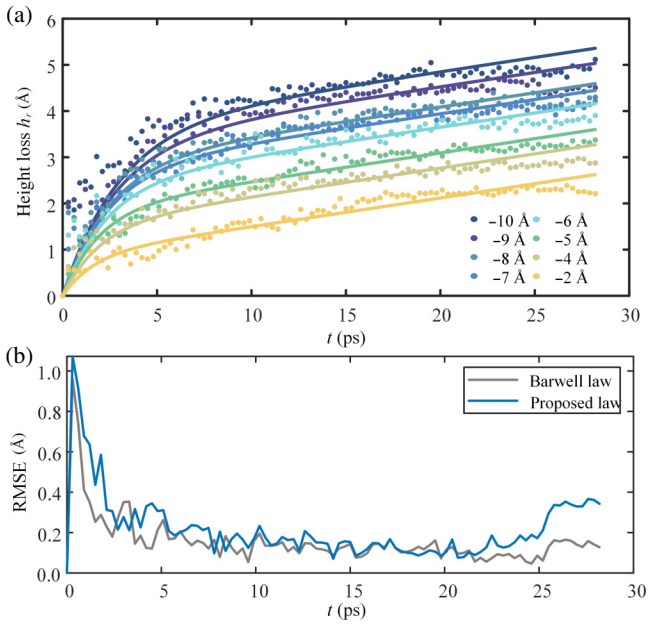

FIG. 8. Evaluation results of height loss with proposed law. (a) Variation in height loss of the head during sliding obtained from MD simulations (solid points) for various head-disk interferences, along with the fitting curves obtained by applying the proposed law (solid lines). (b) Comparison of root-mean-square errors (RMSEs) between the Barwell law and proposed law.

sliding continues and the interaction between the head and substrate acts as an attractive adhesion stress. Interestingly, the normal stress approaches a constant at the end, indicated by the black dotted line in Fig. 7(a). The mean equivalent normal stress of all head-disk interference within the last 10 ps, represented by σ_n^c, is calculated, and the mean stress of each case is also calculated, as shown in Fig. 7(b). σ_n^c is applied to represent the stress between the head and substrate in the steady state.

Thus, Eq. (1) can be rewritten as follows:

$$h(t) = \frac{Kv\sigma_n^0}{p_m}\tau\left[1-\exp\left(-\frac{t}{\tau}\right)\right] + \omega_s^c t,$$
$$\omega_s^c = k_s k_0 \exp\left(-\frac{\Delta U_{\mathrm{act}} - \sigma_n^c \Delta V_{\mathrm{act}}}{K_B T}\right) + k_b. \tag{6}$$

For the DLC sliding process, the parameters K, p_m, k_0, v, ΔU_{act}, ΔV_{act}, and $K_B T$ can be regarded as constants. Therefore, Eq. (5) is expressed as follows:

$$h(t) = B\sigma_n^0\tau\left[1-\exp\left(-\frac{t}{\tau}\right)\right] + \omega_s^c t, \tag{7}$$

where B and ω_s^c are constant. As indicated by the derivation process, the proposed expression is suitable for evaluating plastic wear to atomic wear, which includes the wear-in and steady states.

The methods of obtaining the values of B and ω_s^c are shown in Figs. 14–16 in Appendix C. This law is derived from the clear fundamental physical and chemical debris-level origins of the MD simulation. Furthermore, it establishes a connection between the measurable quantity, that is, normal stress, and height loss. Moreover, the proposed law can be applied to evaluate the wear under time-dependent loads by using the factor of τ compared to the nonempirical law in Ref. [42].

To obtain the initial normal stress, the system is maintained in thermal equilibrium before sliding starts, and the mean stress is calculated as the initial normal stress σ_n^0 of the sliding process, which is listed in Table I. The values

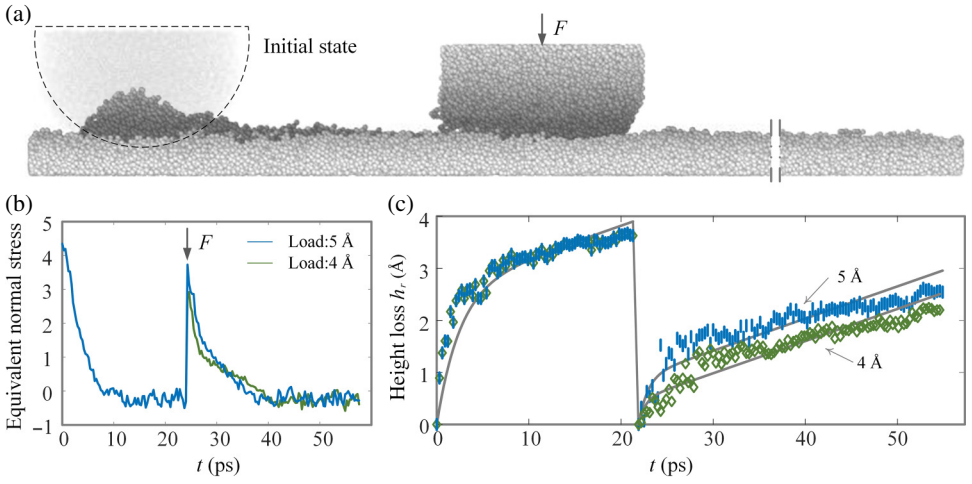

FIG. 9. Verification results of the proposed wear evaluation law. (a) Schematic diagram of the simulation for random loading. (b) Variation of normal stress during sliding. (c) Wear estimation application of the proposed law (solid line) on MD simulation (blue and green markers).

of the other parameters are also given in the table. The proposed law is applied to estimate the head's height loss and the results are shown in Fig. 8. As seen, the head's height losses are also well described by Eq. (7). To compare the accuracy of wear evaluation between the proposed law and the Barwell law, the root-mean-square errors (RMSEs) are calculated. The average RMSE of all interference cases is obtained for each time, and the results are plotted in Fig. 8(b). As can be seen, the ability of the proposed law to estimate wear is comparable with that of the Barwell law.

Additional wear simulations are performed for further verification. A longer DLC substrate is built. At the beginning of sliding, the head-disk interference is set to −8 Å and the head starts to slide for a distance of 120 Å. Then, different additional normal loads are applied to the head to reduce the head-disk interference by 4 and 5 Å, respectively. Thereafter, the head continues to slide. A schematic diagram of the simulation process is shown in Fig. 9(a). The equivalent normal stress and height loss of the head are also calculated, as plotted in Figs. 9(b) and 9(c). However, to better compare the sliding processes before and after load application, results of the pressing process are not given in the figures. According to Fig. 9(b), stress increases when load is applied to the head, and then it decreases as sliding continues. The gradual-steady stress values of the two sliding processes approach a constant and are almost equal, which reconfirms our conclusion. The initial stresses after loading are obtained and applied to Eq. (6), along with the values of the parameters B and ω_s^c in Table I, to estimate the head's height loss, as illustrated in Fig. 9(c). For the first sliding period (from 0 to about 22 ps, before loading), the proposed law agrees well with the MD data. For the second period (from 22 ps to the end, after loading), the head has been sheared and the initial shape is irregular. The proposed law also agrees well with the MD data, indicating that, as a wear law, it is independent of the initial shape of the worn body. As seen, the proposed wear law is more likely to be applied at the nanoscale in practice compared with traditional empirical wear laws.

IV. CONCLUSION

In this paper, a wear estimation method applied at the nanoscale is investigated. A wear model for a DLC head is established using molecular dynamics. The debris-level origins of a DLC head's wear mechanism are analyzed in this simulation. The spatial distribution of wear debris indicates that the atomic wear mechanism leads to the failure of Archard's law after a certain sliding distance. In the sliding process dominated by atomic wear, the normal attractive stress between the head and the substrate is nearly the same and constant, and it is not affected by the initial head-disk interference. An improved wear law based on the debris-level origins is proposed to evaluate time-dependent wear at the nanoscale. This law is derived from the clear fundamental physical and chemical origins of the MD simulation. It establishes a connection between a measurable quantity and height loss compared to the empirical Barwell law. The proposed law is verified by performing additional simulations with different applied loads, and it shows greater applicability in practice.

ACKNOWLEDGMENTS

This study was supported by the National Natural Science Foundation of China (Grant No. 52375124).

APPENDIX A: DETAILS OF MODELING APPROACH

The parallel algorithms (LAMMPS) [43] are adopted to perform the MD simulations in the manuscript. As shown in Fig. 10, the hemispherical DLC head slides on the DLC substrate. Reliable force fields should be chosen carefully for MD simulations. In our study, the many-body Tersoff potential [40] is employed to calculate the interaction between the carbon atoms of the amorphous DLC for both the head and substrate.

The DLC maintains excellent performance of both diamond and graphite due to the bonds between those carbon atoms, mainly the sp^2 and sp^3 bonds in the structure. For MD simulations, the liquid quenching technique [28–30] is usually applied to model the amorphous DLC. At first, the sample is heated from 300 to 2000 K, then it is thermally equilibrated for 10 ps. Later, the sample is heated in temperature increments of 4000 K and is equilibrated for 10 ps at each temperature step. Then the sample is cooled at a quenching rate of 1000 K/ps from 10 000 K down to 300 K. All processes mentioned are in the *NVT* ensemble with temperature controlled by Nose-Hoover chain method.

Finally, the internal residual stress is reduced by adjusting the pressure to 0 in the *NPT* ensemble. The results of the radial distribution function and the stress-strain for the sample, obtained by the tensile test, are sketched in

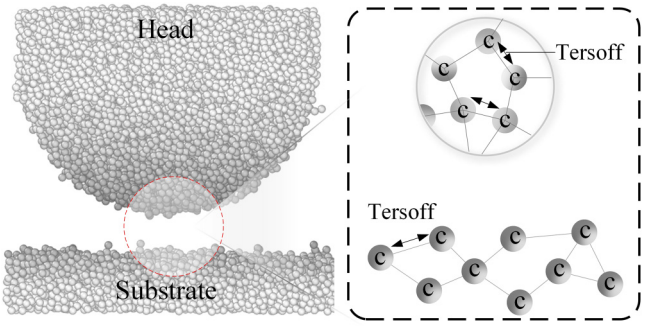

FIG. 10. Simulation model of the head-substrate system and the interaction force field between those atoms.

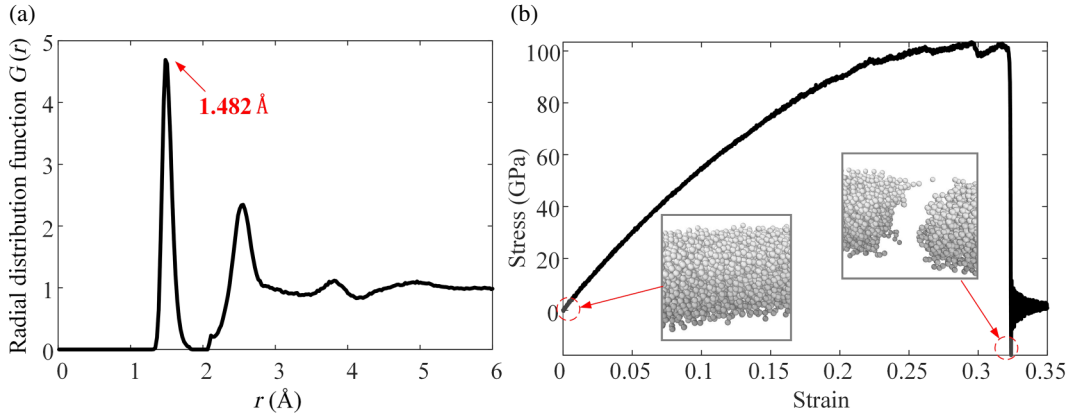

FIG. 11. Performance of DLC. (a) The radial distribution function of the final sample. (b) Stress-strain curve of tensile test for the sample.

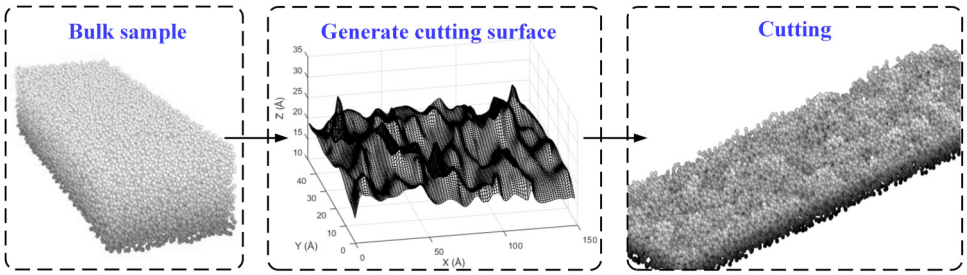

FIG. 12. The "cutting" method in our work. At first, a large enough cuboid bulk DLC sample is modeled with the liquid quenching technique. Then a rough surface composed of discrete coordination points is generated whose height follows the Gaussian distribution with a standard deviation $\sigma = 1.5$ Å. (It is the same for the hemispherical surface whose radius R is 30 Å). Later, the cutting method is applied to the bulk sample: i.e., if the position of the sample is under the generated rough surface (inside the hemisphere for the head), this atom is retained, otherwise it is removed.

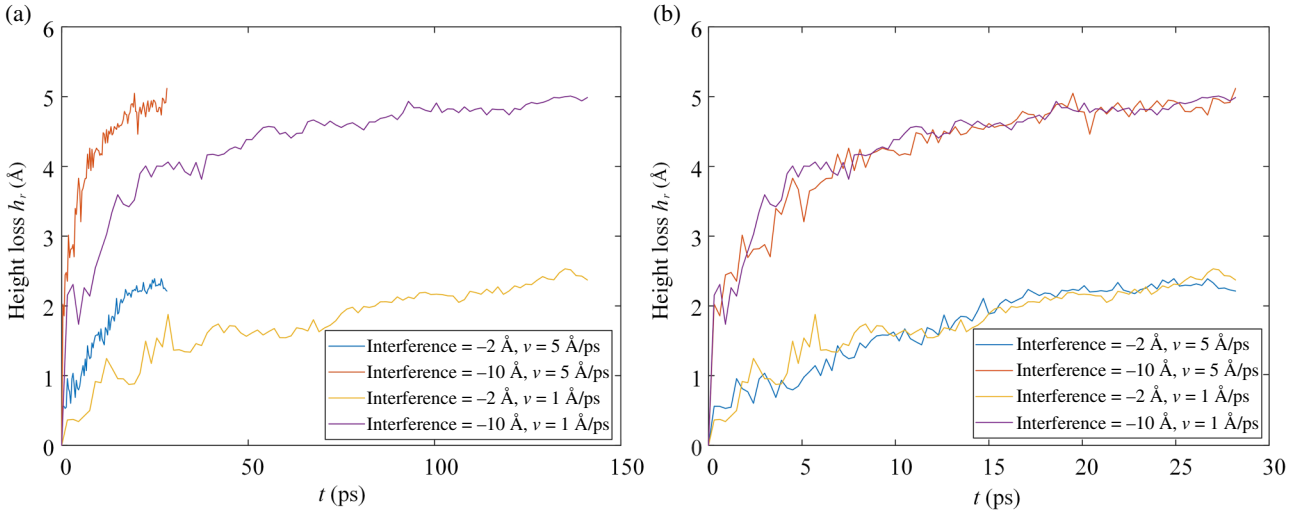

FIG. 13. The height loss of 5 Å/ps and 1 Å/ps. The minimum head-disk interference of the simulations is −2 Å and the maximum head-disk interference is −10 Å. (a) The original height loss over time. (b) The height loss for the simulation of $v = 1$ Å/ps with the X coordinate compressed for better comparison.

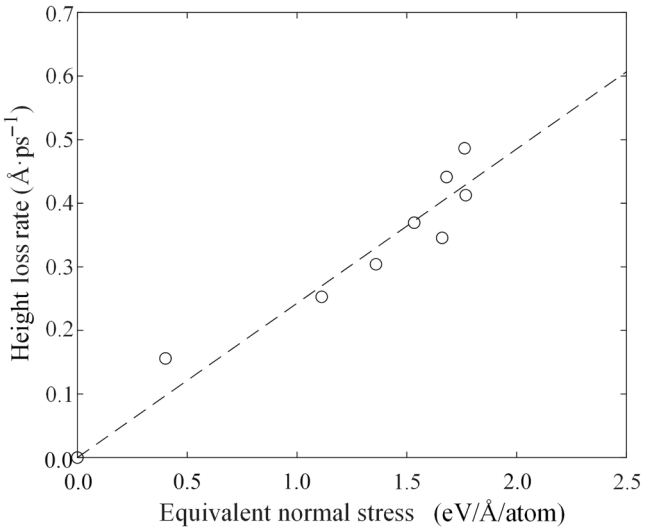

FIG. 14. Fitting results with MD simulations for Eq. (3) by using $B = Kv/p_m = 0.2427$.

Fig. 11. As shown, the radial distance (r) of the first-nearest-neighbor peak is 1.485 Å and the Young's modulus, calculated when the strain is 0.15 (still deforming elastically), is about 497 GPa, both of which indicate the reliability of the DLC model for its comparability to Ref. [29].

Because the phase transformation (heating/quenching) during the modeling of DLC leads to a failure to maintain the initial shape (e.g., hemispherical), it is hard to obtain the hemispherical DLC head sample and DLC substrate sample with a rough surface directly in LAMMPS. Here, we propose a "cutting" method, i.e., a sample of any shape can be obtained so long as we cut it from a bulk sample, as shown in Fig. 12, to prepare the samples needed in the work. All the cutting samples are relaxed and we get a rough substrate with dimensions $200 \times 60 \times 10$ Å^3 (average height with 1.5 Å standard deviation) and a head (a hemisphere with radius of 30 Å attached to a cylinder with a height of 15 Å).

APPENDIX B: INFLUENCE OF THE HORIZONTAL VELOCITY ON HEIGHT LOSS

The enterprise HDD speeds can reach 15 000 rpm. For the 3.5-inch HDD, the speed of the disk can reach about 150 m/s. The velocity 500 m/s is used in the paper to shorten the simulation time. We compare the height loss for the velocity 500 m/s (5 Å/ps) to the results for 100 m/s (1 Å/ps) to discuss the influence of the velocity, as shown in Fig. 13. As seen in the Fig. 2(a), when the velocity is 1 Å/ps, the height loss also experiences the wear-in and steady state, so the proposed method in our paper can be applied in the evaluation of head wear. Then, for better comparison, the value of the X coordinate for the simulation of $v = 1$ Å/ps is divided by 5. When the velocity of 5 Å/ps is used, it has little influence on the process of height loss for different head-disk interferences in our paper. So, it is appropriate to apply the velocity of 5 Å/ps for a shorter simulation time.

APPENDIX C

When the sliding speed remains constant, ω_w is as a function of σ_n with a constant coefficient, as shown in Eq. (3). As analyzed in the paper, the initial stage is dominated by plastic wear, so we still use the simulation

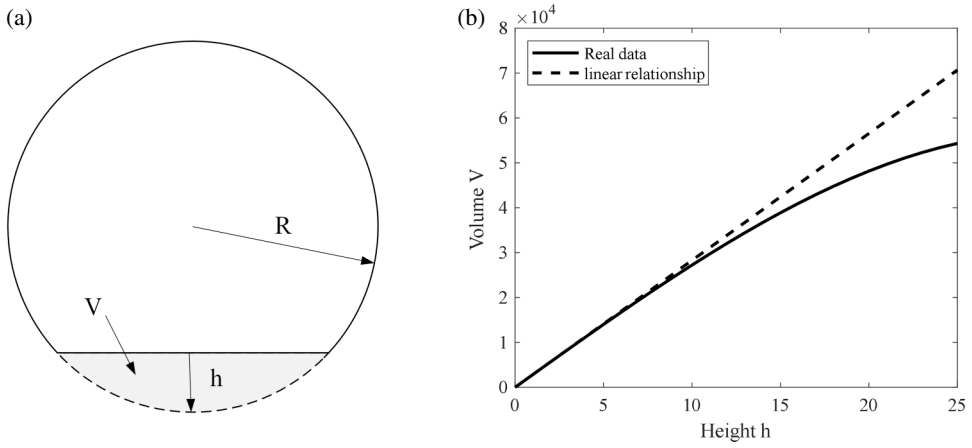

FIG. 15. The relationship between the height and the volume for a ball segment. (a) R is the radius of the ball and its value is 30 Å, h is the height, and V is the volume of the ball segment, although the illustration shows a circle. (b) Comparison between of the true relationship and the linear relationship between h and V.

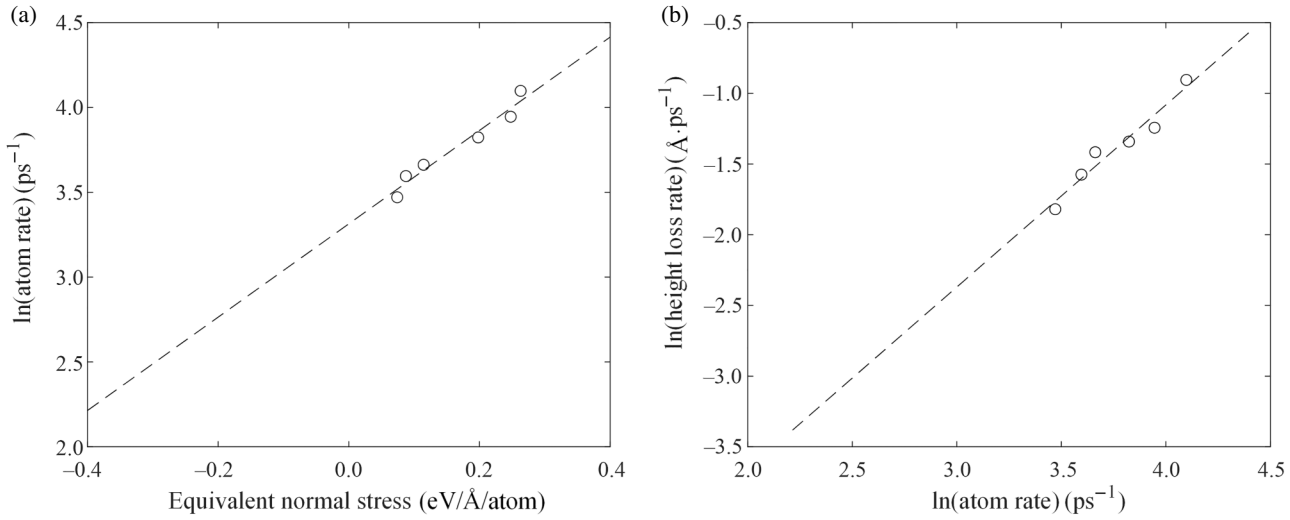

FIG. 16. Fit parameters used in Eqs. (4) and (5). (a) Fitting results by using $\Delta U_{\text{act}} = 0.1524$ and $\Delta V_{\text{act}} = 0.07112$. (b) Fitting results by using $\ln(k_s) = 1.288$ and $\ln(k_b) = -6.234$.

data from the article to fit and obtain the values of the coefficients. The result is shown in Fig. 14 (Fig. 15).

Additional simulations are conducted to obtain the estimates for ΔU_{act} and ΔV_{act} in Eq. (4) in the main text. The prefactor k_0 takes a value of 10^{14} [42,44], and $K_B = 1.380649 \times 10^{-23}$ J/K and $T = 300$ K are also employed in this work. The stress is taken as an average value, and the number of worn loss atoms is used in logarithmic form. The estimation for k_s used in Eq. (5) is also obtained by fitting. The results are shown in Fig. 16.

[1] T. Kunze, S. Gemming, M. Posselt, and G. Seifert, Tribological aspects of carbon-based nanocoatings – Theory and simulation, Z. Phys. Chem. **225**, 379 (2011).

[2] K. Ono, Numerical simulation of thermal fly-height control slider touchdown test for achieving ideal subnanometer clearance head slider touchdown behaviors, Tribol. Lett. **68**, 44 (2020).

[3] John T. Burwell Jr., Survey of possible wear mechanisms, Wear **1**, 119 (1957).

[4] R. Holm, *Electric Contacts Handbook* (Springer, Berlin, Heidelberg, 1958).

[5] J. F. Archard, Contact and rubbing of flat surfaces, J. Appl. Phys. **24**, 981 (1953).

[6] R. Liu and D. Y. Li, Modification of Archard's equation by taking account of elastic/pseudoelastic properties of materials, Wear **251**, 956 (2001).

[7] R. Aghababaei and K. Zhao, Micromechanics of material detachment during adhesive wear: A numerical assessment of Archard's wear model, Wear **476**, 203739 (2021).

[8] M. Schewe, H. Wilbuer, and A. Menzel, Simulation of wear and effective friction properties of microstructured surfaces, Wear **464**, 203491 (2021).

[9] J. J. Liu, J. K. Notbohm, R. W. Carpick, and K. T. Turner, Method for characterizing nanoscale wear of atomic force microscope tips, ACS Nano **4**, 3763 (2010).

[10] G. Y. Deng, Y. Chong, L. H. Su, L. H. Zhan, P. T. Wei, X. Zhao, L. Zhang, Y. Z. Tian, H. T. Zhu, and N. Tsuji, Mechanisms of remarkable wear reduction and evolutions of subsurface microstructure and nano-mechanical properties during dry sliding of nano-grained Ti_6Al_4V alloy: A comparative study, Tribol. Int. **169**, 107464 (2022).

[11] H. Bhaskaran, B. Gotsmann, A. Sebastian, U. Drechsler, M. A. Lantz, M. Despont, P. Jaroenapibal, R. W. Carpick, Y. Chen, and K. Sridharan, Ultralow nanoscale wear through atom-by-atom attrition in silicon-containing diamond-like carbon, Nat. Nanotechnol. **5**, 181 (2010).

[12] K. Y. E. Awwad, B. F. Yousif, K. Fallahnezhad, K. Saleh, and X. S. Zeng, Influence of graphene nanoplatelets on mechanical properties and adhesive wear performance of epoxy-based composites, Friction **9**, 856 (2021).

[13] R. A. Bernal and R. W. Carpick, Visualization of nanoscale wear mechanisms in ultrananocrystalline diamond by in-situ TEM tribometry, Carbon **154**, 132 (2019).

[14] T. Tabrizi, H. Aghajani, H. Saghafian, and F. F. Laleh, Correction of Archard equation for wear behavior of modified pure titanium, Tribol. Int. **155**, 106772 (2021).

[15] H. C. Meng and K. C. Ludema, Wear models and predictive equations: Their form and content, Wear **181**, 443 (1995).

[16] K. Zhao and R. Aghababaei, Adhesive wear law at the single asperity level, J. Mech. Phys. Solids **143**, 104069 (2020).

[17] J. Hu, H. Song, S. Sandfeld, X. Liu, and Y. Wei, Breakdown of Archard law due to transition of wear mechanism from plasticity to fracture, Tribol. Int. **173**, 107660 (2022).

[18] J. J. Liu, Y. J. Jiang, D. S. Grierson, K. Sridharan, Y. C. Shao, T. D. B. Jacobs, M. L. Falk, R. W. Carpick, and K. T. Turner, Tribochemical wear of diamond-like carbon-coated atomic force microscope tips, ACS Appl. Mater. Interfaces **9**, 35341 (2017).

[19] Y. Wang, N. Yamada, J. X. Xu, J. Zhang, Q. Chen, Y. Ootani, Y. Higuchi, N. Ozawa, M. I. D. Bouchet, J. M. Martin, *et al.*, Triboemission of hydrocarbon molecules from diamond-like carbon friction interface induces atomic-scale wear, Sci. Adv. **5**, 1 (2019).

[20] A. Al-Azizi, O. Eryilmaz, A. Erdemir, and S. H. Kim, Surface structure of hydrogenated diamond-like carbon: Origin of run-in behavior prior to superlubricious interfacial shear, Langmuir **31**, 1711 (2015).

[21] J. Hilbert, F. Mangolini, J. B. Mcclimon, J. R. Lukes, and R. W. Carpick, Si doping enhances the thermal stability of diamond-like carbon through reductions in carbon-carbon bond length disorder, Carbon **131**, 72 (2018).

[22] M. R. Price and B. Raeymaekers, Quantifying adhesion of ultra-thin multi-layer DLC coatings to Ni and Si substrates using shear, tension, and nanoscratch molecular dynamics simulations, Acta Mater. **141**, 317 (2017).

[23] L. C. Bai, N. Srikanth, E. A. Korznikova, J. A. Baimova, S. V. Dmitriev, and K. Zhou, Wear and friction between smooth or rough diamond-like carbon films and diamond tips, Wear **372**, 12 (2017).

[24] L. Dai, V. Sorkin, and Y. W. Zhang, Effect of surface chemistry on the mechanisms and governing laws of friction and wear, ACS Appl. Mater. Interfaces **8**, 8765 (2016).

[25] L. C. Bai, N. Srikanth, H. Wu, Y. Liu, B. Liu, and K. Zhou, Investigation on tensile behaviors of diamond-like carbon films, J. Non-Cryst. Solids **443**, 8 (2016).

[26] Y. G. Gogotsi, A. Kailer, and K. G. Nickel, Transformation of diamond to graphite, Nature **401**, 663 (1999).

[27] Z. D. Sha, V. Sorkin, P. S. Branicio, Q. X. Pei, Y. W. Zhang, and D. J. Srolovitz, Large-scale molecular dynamics simulations of wear in diamond-like carbon at the nanoscale, Appl. Phys. Lett. **103**, 1174 (2013).

[28] N. A. Marks, Evidence for subpicosecond thermal spikes in the formation of tetrahedral amorphous carbon, Phys. Rev. B **56**, 2441 (1997).

[29] Z. D. Sha, P. S. Branicio, Q. X. Pei, V. Sorkin, and Y. W. Zhang, A modified Tersoff potential for pure and hydrogenated diamond-like carbon, Comp. Mater. Sci. **67**, 146 (2013).

[30] P. Wei, M. Y. He, and W. B. Ao, Molecular dynamics study of the frictional behaviors of diamond-like carbon films, Appl. Phys. A **127**, 652 (2021).

[31] S. Rajauria, S. V. Canchi, E. Schreck, and B. Marchon, Nanoscale wear and kinetic friction between atomically smooth surfaces sliding at high speeds, Appl. Phys. Lett. **106**, 275 (2015).

[32] Stukowski, Visualization and analysis of atomistic simulation data with OVITO–the Open Visualization Tool, Modell. Simul. Mater. Sci. Eng. **18**, 2154 (2010).

[33] Y. J. Yang, L. P. Huang, and Y. F. Shi, Adhesion suppresses atomic wear in single-asperity sliding, Wear **352–353**, 31 (2016).

[34] S. J. Eder, G. Feldbauer, D. Bianchi, U. Cihak-Bayr, G. Betz, and A. Vernes, Applicability of macroscopic wear and friction laws on the atomic length scale, Phys. Rev. Lett. **115**, 025502 (2015).

[35] R. Colaco and A. P. Serro, Nanoscale wear of hard materials: An overview, Curr. Opin. Colloid Interface Sci. **47**, 118 (2020).

[36] Gotsmann and M. A. Lantz, Atomistic wear in a single asperity sliding contact, Phys. Rev. Lett. **101**, 125501 (2008).

[37] T. D. B. Jacobs and R. W. Carpick, Nanoscale wear as a stress-assisted chemical reaction, Nat. Nanotechnol. **8**, 108 (2013).

[38] Y. Wang, J. Qin, J. X. Xu, J. H. Sun, L. Chen, L. M. Qian, and M. Kubo, Definition of atomic-scale contact: What dominates the atomic-scale friction behaviors?, Langmuir **38**, 11699 (2022).

[39] Y. F. Mo, K. T. Turner, and I. Szlufarska, Friction laws at the nanoscale, Nature **457**, 1116 (2009).

[40] J. Tersoff, Modeling solid-state chemistry: Interatomic potentials for multicomponent systems, Phys. Rev. B **39**, 5566 (1989).

[41] F. T. Barwell, Wear of metals, Wear **1**, 317 (1958).

[42] Y. Wang, J. X. Xu, Y. Ootani, N. Ozawa, K. Adachi, and M. Kubo, Non-empirical law for nanoscale atom-by-atom wear, Adv. Sci. **8**, 2002827 (2021).

[43] S. Plimpton, Fast parallel algorithms for short-range molecular-dynamics, J. Comput. Phys. **117**, 1 (1995).

[44] Y. C. Shao, T. D. B. Jacobs, Y. J. Jiang, K. T. Turner, R. W. Carpick, and M. L. Falk, Multibond model of single-asperity tribochemical wear at the nanoscale, ACS Appl. Mater. Interfaces **9**, 35333 (2017).